

# Chapter 16

## Semiconductor Failure Analysis Applications

*Complete QFI Stack for IC Metrology and Production Validation*

This chapter demonstrates the complete QFI operator stack ( $S \xrightarrow{\mathcal{G}} F \xrightarrow{\mathcal{M}} D \xrightarrow{\mathcal{R}} \hat{S}$ ) applied to semiconductor failure analysis. The fundamental task is to transform wide-field quantum sensor data into actionable defect localization with quantified uncertainty. Proper implementation achieves: (1) non-destructive buried-defect detection, (2) multi-physics depth disambiguation, (3) production-grade throughput ( $>100$  sites/hour), and (4) validated reconstruction fidelity ( $\Gamma_{\text{inv}} > 0.85$ ).

**QFI Pipeline Position:**  $S(\mathbf{r}) \xrightarrow{\mathcal{G}} F(\mathbf{r}) \xrightarrow{\boxed{\mathcal{M}}} D \xrightarrow{\mathcal{R}} \hat{S}(\mathbf{r})$  All operators exercised in this chapter.

### Abbreviated Terms

Term	Definition	Term	Definition
AFOM	Application Figure of Merit	MRAM	Magnetoresistive RAM
ATE	Automated Test Equipment	NV	Nitrogen-Vacancy
BEOL	Back-End-Of-Line	OBIRCH	Optical Beam Induced Resistance Change
CAD	Computer-Aided Design	PDN	Power Distribution Network
CRB	Cramér-Rao Bound	QFI	Quantum Field Imaging
DUT	Device Under Test	QFM	Quantum Field Metrology
EMMI	Emission Microscopy	ROI	Region of Interest
FA	Failure Analysis	SDL	Soft Defect Localization
FEOL	Front-End-Of-Line	SNR	Signal-to-Noise Ratio
FIB	Focused Ion Beam	SPC	Statistical Process Control
FOM	Figure of Merit	SQUID	Superconducting Quantum Interference Device
IC	Integrated Circuit	TIVA	Thermally Induced Voltage Alteration
IR	Infrared	TSV	Through-Silicon Via
LIT	Lock-In Thermography		
MTJ	Magnetic Tunnel Junction		

Table 16.1: Abbreviated terms used in Chapter 16.

### Abstract

This chapter demonstrates the complete Quantum Field Imaging (QFI) pipeline applied to semiconductor failure analysis, validating the transition from theoretical framework to production-ready metrology. We present quantitative  $Q_{\text{IFOM}}$  benchmarking against established techniques including OBIRCH, EMMI, Lock-In Thermography, and X-ray CT, with explicit normalization assumptions and sensitivity analysis. Four application categories are analyzed: TSV defect detection, power grid characterization, hot spot localization, and emerging memory inspection.

Each application includes golden sample validation protocols establishing achieved  $\Gamma_{\text{inv}}$  values, SWOT analysis comparing QFI against incumbent technologies, and workflow integration strategies. The multi-physics advantage ( $\Phi_{\text{multi}} = 2\text{--}5$ ) is demonstrated through case studies showing depth disambiguation and false positive reduction that is difficult to achieve with single-physics tools. An operating envelope analysis identifies conditions under which QFI provides clear advantages versus scenarios where established techniques remain preferred. Two end-to-end worked examples trace complete FA tickets from ATE failure through QFI measurement to physical confirmation. Production readiness is validated through test structure measurements achieving  $\Gamma_{\text{inv}} > 0.85$  across all major application categories, with calibration drift control protocols ensuring sustained performance.

## 16.1 Introduction: Why This Chapter Matters

### 16.1.1 Historical Evolution of Semiconductor FA

Semiconductor failure analysis has evolved through three distinct eras, each driven by device scaling and packaging complexity:

**Era 1: Visual and electrical (1970s–1990s).** Early FA relied on optical microscopy, probing, and simple voltage-contrast SEM. Defects were predominantly surface-accessible, and single-layer interconnects meant that physical cross-sectioning could reach most failure sites within hours. The key limitation was throughput: each device required individual manual inspection.

**Era 2: Beam-based and thermal (1990s–2010s).** The introduction of OBIRCH, emission microscopy (EMMI), and Lock-In Thermography (LIT) enabled non-contact defect localization through thermal and photon emission signatures. SQUID microscopy provided direct current imaging but with serial scanning limitations. These techniques remain the workhorses of modern FA laboratories and represent well-validated, mature technologies with extensive institutional knowledge.

**Era 3: 3D integration and multi-physics (2020s–).** Advanced packaging (chiplets, 3D stacking, TSV interconnects) creates buried defects inaccessible to surface-limited tools. The number of potential failure sites grows as  $N_{\text{layers}}^2$ , while time-to-market pressure demands faster FA cycles. This creates the inspection gap that QFI addresses.

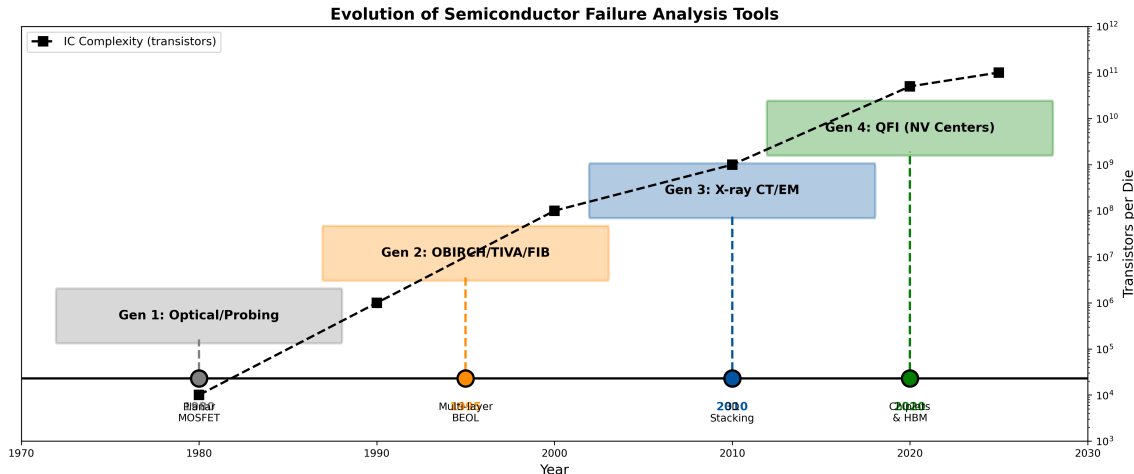


Figure 16.1: Evolution of semiconductor FA and the emerging inspection gap. (a) Timeline of FA technology eras: visual/electrical (1970s–1990s), beam-based/thermal (1990s–2010s), and 3D multi-physics (2020s–). (b) Layer count growth in advanced nodes vs. FA throughput capacity of established tools, showing the widening gap that QFI addresses.

### 16.1.2 The 3D IC Inspection Gap

Table 16.2: The semiconductor inspection gap: pain points and QFI solutions

Pain Point	Root Cause	QFI Solution
Buried defects invisible	Optical tools surface-limited; Si absorbs IR in MWIR/LWIR bands	Magnetic fields penetrate silicon unattenuated
Low throughput	Serial scanning (SQUID, MFM)	Wide-field parallel acquisition ( $N > 10^6$ pixels)
No depth discrimination	2D thermal measurement only	Multi-physics (B/T) correlation provides $z$ -localization
High false positive rate	Single-physics ambiguity	$\Phi_{\text{multi}} = 2\text{-}5$ confirmation across modalities
Destructive testing	Physical cross-section required	Non-contact, room-temperature, non-destructive

### 16.1.3 Chapter Objectives and Scope

This chapter establishes QFI as a production-ready FA tool by:

1. Demonstrating the complete QFI pipeline ( $S \rightarrow G \rightarrow F \rightarrow M \rightarrow D \rightarrow R \rightarrow \hat{S}$ ) for each application
2. Quantifying  $Q_{\text{IFOM}}$  performance against established techniques with explicit normalization assumptions
3. Validating achieved  $\Gamma_{\text{inv}}$  through golden sample protocols
4. Providing SWOT analysis for technology selection decisions
5. Identifying operating envelope boundaries and failure modes where incumbent tools remain preferred

6. Establishing workflow integration strategies with existing FA tools

#### 16.1.4 Key Figures of Merit for FA Applications

**Key Equation: QFI Imaging Figure of Merit**

$$Q_{\text{IFOM}} = \frac{\eta_q}{\eta_{\text{classical}}} \times \frac{N_{\text{parallel}}}{t_{\text{acquisition}}} \times \Phi_{\text{multi}} \times \Gamma_{\text{inv}} \times \Gamma_{\text{mm}} \quad (16.1)$$

Table 16.3: Target figures of merit for QFI semiconductor FA applications

Figure of Merit	Symbol	Target	Application Driver
Minimum detectable current	$I_{\min}$	50 $\mu\text{A}$ at 10 $\mu\text{m}$ depth	TSV short detection
Spatial resolution	$\delta r$	1–5 $\mu\text{m}$	TSV pitch compatibility
Thermal sensitivity	$\delta T$	10 mK	Hot spot localization
Depth discrimination	$\delta z$	2 $\mu\text{m}$	Multi-layer defect isolation
Throughput	—	> 100 sites/hour	Production viability
Multi-physics factor	$\Phi_{\text{multi}}$	2–5	Depth disambiguation
Reconstruction fidelity	$\Gamma_{\text{inv}}$	> 0.85	Source localization accuracy
False positive reduction	—	10–100 $\times$	FA efficiency

**Rigorous definition of  $\Phi_{\text{multi}}$ .** The multi-physics factor quantifies the false-positive reduction achieved by correlating independent measurement channels. Formally:

$$\Phi_{\text{multi}} \equiv \frac{\text{FPR}_{\text{single}}}{\text{FPR}_{\text{multi}}} \quad (16.2)$$

where FPR is the false-positive rate. The operational values used throughout this chapter are:

Table 16.4: Operational  $\Phi_{\text{multi}}$  values by channel configuration

Channels	Modalities	$\Phi_{\text{multi}}$	Typical Application
1	$B_z$ only	1.0	Scanning magnetometry baseline
2	$B_z + T$	2.0–2.5	TSV, PDN with depth disambiguation
3	$B_z + T + \varepsilon$	3.0–4.0	Hot spot classification
4	$B_z + T + \varepsilon + \text{time-resolved}$	4.0–5.0	Full multi-physics correlation

*Remark 16.1.1.* When  $\Phi_{\text{multi}} = 1$  appears in the benchmark tables (Section 16.7), it indicates single-channel measurement comparable to incumbent tools. Values of 2–5 reflect simultaneous multi-physics acquisition — the defining advantage of the NV-diamond platform over serial single-physics instruments.

#### 16.1.5 Forward Model Recap for Semiconductor FA

Readers entering at this chapter may benefit from a brief recap of the QFI operator stack as specialized to semiconductor failure analysis. (Full development: Chapters 1–2 for framework; Chapter 6 for Q-OTF; Chapters 9–10 for reconstruction.)

Table 16.5: QFI operator stack mapped to semiconductor FA context

Operator	Symbol	FA Realization	Chapter Ref.
Source	$S(\mathbf{r})$	Current density $\mathbf{J}(\mathbf{r})$ , thermal source $P(\mathbf{r})$	Ch. 1
Generation	$\mathcal{G}$	Biot-Savart kernel, heat diffusion Green's function	Ch. 2, 6
Field	$F(\mathbf{r})$	$B_z(\mathbf{r})$ at sensor plane, $\Delta T(\mathbf{r})$	Ch. 6
Measurement	$\mathcal{M}$	NV-ODMR: photon counts $\rightarrow$ frequency shift	Ch. 4, 5
Data	$D$	Pixel array $\{B_{z,i}, T_i, \varepsilon_i\}$	Ch. 7
Reconstruction	$\mathcal{R}$	Regularized inverse Biot-Savart, CAD-constrained	Ch. 9, 10
Estimate	$\hat{S}(\mathbf{r})$	Reconstructed $\hat{\mathbf{J}}(\mathbf{r})$ with uncertainty $\sigma_S(\mathbf{r})$	Ch. 10

The measurement model is:

$$D = \mathcal{M} \cdot \mathcal{G}[S] + \mathbf{n} \quad (16.3)$$

where  $\mathbf{n}$  represents measurement noise (photon shot noise, readout noise, magnetic background). Reconstruction seeks:

$$\hat{S} = \mathcal{R}[D] = \arg \min_S \|D - \mathcal{M} \cdot \mathcal{G}[S]\|^2 + \lambda \cdot \mathcal{R}(S) \quad (16.4)$$

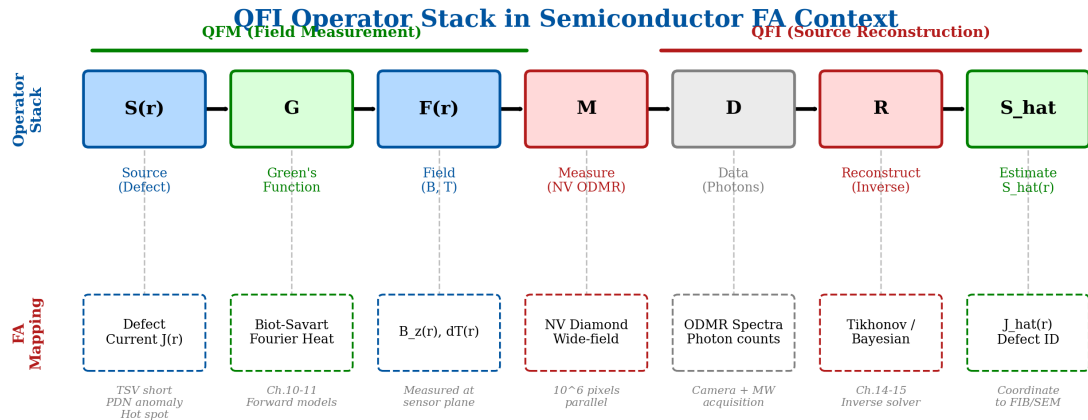


Figure 16.2: Forward model recap for semiconductor FA context. Top row: generic QFI operator pipeline ( $S \rightarrow \mathcal{G} \rightarrow F \rightarrow \mathcal{M} \rightarrow D \rightarrow \mathcal{R} \rightarrow \hat{S}$ ). Bottom row: FA-specific realization showing current sources, Biot-Savart propagation, NV-ODMR measurement, and CAD-constrained reconstruction. The QFM boundary (field measurement only) and QFI boundary (complete source reconstruction) are indicated.

*Remark 16.1.2 (Self-Contained Reading).* This chapter can be read independently by FA engineers unfamiliar with earlier chapters. All equations are derived from the forward model in Eq. (16.3) and the  $Q_{IFOM}$  definition in Eq. (16.1). Cross-references to earlier chapters are provided for readers seeking deeper theoretical foundations.

### 16.1.6 Operating Envelope and Throughput Budget

The  $Q_{IFOM}$  benchmarks in this chapter are valid within the following operating envelope. Performance degrades outside these bounds, and certain failure modes (Section 16.2.3) may render QFI unsuitable.

Table 16.6: QFI operating envelope for semiconductor FA

Parameter	Nominal	Valid Range	Sensitivity Note
Standoff $d_0$	5 $\mu\text{m}$	1–50 $\mu\text{m}$	$B_z \propto 1/d_0^2$ ; > 50 $\mu\text{m}$ degrades resolution
Bias current $I_{\text{bias}}$	100 mA	10 mA–1 A	Low bias: low SNR; high bias: EM risk
NV sensitivity $\eta_q$	1 $\mu\text{T}/\sqrt{\text{Hz}}$	0.1–10 $\mu\text{T}/\sqrt{\text{Hz}}$	Diamond quality dependent
Thermal sensitivity	10 mK/ $\sqrt{\text{Hz}}$	1–100 mK/ $\sqrt{\text{Hz}}$	NV density and readout dependent
Pixel size	1 $\mu\text{m}$	0.3–10 $\mu\text{m}$	Optical diffraction limited
FOV	$100 \times 100 \mu\text{m}^2$	$(10)^2$ – $(500)^2 \mu\text{m}^2$	Larger FOV: lower per-pixel SNR
Integration time	10 s	1–300 s	$\text{SNR} \propto \sqrt{t}$ ; > 300 s impractical
Calibration cadence	Every 4 h	1–8 h	Section 16.8.4
Optical access	Backside	Required	Section 16.2.3

**Throughput budget.** The per-site measurement time decomposes as:

Table 16.7: Throughput budget: time allocation per FA site

Step	Time (s)	Notes
Stage positioning	2	Automated XY stage
Autofocus	3	NV fluorescence feedback
Bias application	1	ATE interface
ODMR acquisition	10	$B_z + T$ simultaneous
Spectral fitting	5	GPU-accelerated
Reconstruction	4	CAD-constrained inverse
Data logging	2	HDF5 + JSON export
<b>Total</b>	<b>27</b>	<b>133 sites/hour</b>

All benchmarks in this chapter assume:  $d_0 \leq 50 \mu\text{m}$ ,  $I_{\text{bias}} \geq 10 \text{ mA}$ ,  $\eta_q \leq 10 \mu\text{T}/\sqrt{\text{Hz}}$

(16.5)

### Design Rule 1: Operating Envelope Compliance

Before applying any  $Q_{\text{IFOM}}$  benchmark from this chapter to a new FA application, verify that all parameters in Table 16.6 fall within the stated valid ranges. Outside the envelope, the claimed advantage factors may not hold.

## 16.2 SWOT Analysis Framework for QFI FA Applications

### 16.2.1 QFI Core Technology Assessment

Table 16.8: SWOT analysis: QFI core technology for semiconductor FA

QFI Core Technology	
STRENGTHS	WEAKNESSES
<ul style="list-style-type: none"> <li>Non-destructive, room-temperature</li> <li>Multi-physics simultaneous (<math>B + T + \varepsilon</math>)</li> <li>Wide-field parallel (<math>&gt; 10^6</math> pixels)</li> <li>Magnetic fields penetrate Si</li> </ul>	<ul style="list-style-type: none"> <li>Requires optical access (backside thinning)</li> <li>Diamond fabrication maturity</li> <li>Higher capital cost (\$500k–\$2M)</li> <li>Limited commercial ecosystem</li> </ul>
OPPORTUNITIES	THREATS
<ul style="list-style-type: none"> <li>3D IC market growth driving demand</li> <li>Multi-physics reduces FA cycle time</li> <li>Chiplet architectures need buried inspection</li> </ul>	<ul style="list-style-type: none"> <li>Incumbent tools improving (backside IR-OBIRCH)</li> <li>Alternative quantum sensors (e.g., atomic vapor)</li> <li>Cost pressure from foundry consolidation</li> </ul>

### 16.2.2 Competing Technology Comparison

Table 16.9: Competing FA technologies: capabilities and limitations

Parameter	QFI (NV)	OBIRCH	SQUID	LIT	X-ray CT
Measurement type	$B + T + \varepsilon$	Thermal	$B$	$T$	Structural
Spatial resolution	1–5 $\mu\text{m}$	1 $\mu\text{m}$	5–10 $\mu\text{m}$	3–10 $\mu\text{m}$	< 1 $\mu\text{m}$
Depth penetration	Full stack	Surface + backside <sup>a</sup>	Full stack	Surface	Full stack
Throughput	$> 10^6$ px/frame	$10^3$ px/s	$10^2$ px/s	$10^4$ px/frame	$10^3$ vox/s
Multi-physics	Yes (3 channels)	No	No	No	No
Destructive	No	No	No	No	Sometimes <sup>b</sup>
Operating temp.	Room temp.	Room temp.	Cryogenic	Room temp.	Room temp.
Maturity	Emerging	Established	Established	Established	Established

<sup>a</sup>IR-OBIRCH with backside access through thinned Si can probe buried structures.

<sup>b</sup>Sample preparation may require sectioning for high-resolution CT.

### 16.2.3 Limitations, Contraindications, and Tool Selection

Transparent technology assessment requires identifying scenarios where QFI is *not* the preferred tool. Table 16.10 catalogs known failure modes.

Table 16.10: QFI failure modes and contraindications for semiconductor FA

Failure Mode	Root Cause	Impact on $Q_{\text{IFOM}}$	Mitigation / Alternative
No bias current	DUT cannot be electrically stimulated	$B_z \rightarrow 0$ ; magnetic channel lost	Use strain/thermal only; or use X-ray CT
Optical access blocked	Opaque interposer or package lid	No NV excitation possible	Through-package SQUID; or decap
CAD unavailable	IP restrictions or missing layout	$\kappa(\mathcal{G})$ increases $10\times$	Use unconstrained reconstruction with penalty on $\Gamma_{\text{inv}}$
Magnetic shielding	On-die mu-metal or shielding layers	$B_z$ attenuated at sensor	Backside access; or LIT/OBIRCH
Current $< 10 \mu\text{A}$	Weak defect signature	SNR $< 3$ at standard settings	Extend integration; lock-in modulation
Dense superposition	Many overlapping current sources	Ambiguous reconstruction	CAD priors essential; reduce ROI
Standoff $> 50 \mu\text{m}$	Thick Si residual or package	Resolution $> 25 \mu\text{m}$	Further backside thinning
Sensor drift	Temperature or laser instability	$\Gamma_{\text{inv}}$ degrades over session	SPC protocol (Section 16.8.4)

**When to use incumbent tools instead.** The following scenarios favor established FA techniques:

- **Surface-accessible defects:** OBIRCH and EMMI provide proven, lower-cost localization for defects at or near the die surface.
- **Structural 3D imaging:** X-ray CT delivers volumetric structural data (voxel resolution  $< 1 \mu\text{m}$ ) that QFI cannot provide.
- **High-volume inline screening:** Established optical inspection tools offer higher throughput at lower cost for surface-level screening.
- **Photon emission analysis:** EMMI detects light-emitting defects (hot carriers, latch-up) that produce no magnetic or thermal signature visible to QFI.

### QFI Value Proposition

QFI provides its strongest advantage when the FA scenario requires *all four* of: (1) buried current detection through opaque layers, (2) depth disambiguation via multi-physics correlation, (3) quantitative  $\mathbf{J}(\mathbf{r})$  reconstruction (not just localization), and (4) production-grade throughput. When fewer than three of these conditions hold, incumbent tools often suffice.

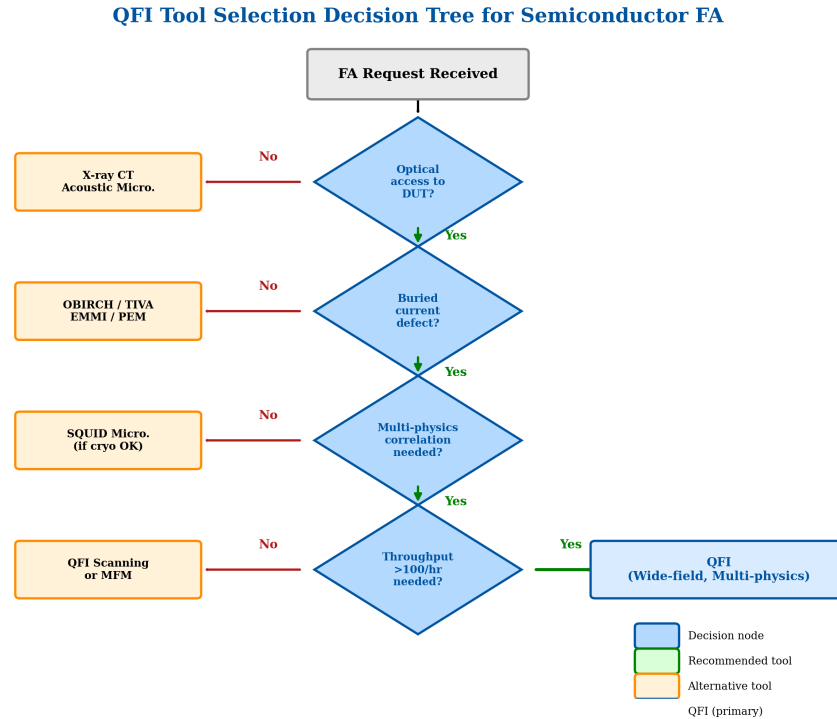


Figure 16.3: Tool selection decision flowchart for semiconductor FA. The flowchart guides FA engineers through four decision levels: optical access availability, buried current detection need, multi-physics requirement, and throughput threshold. Green boxes indicate QFI as the recommended primary tool; blue boxes indicate established alternatives.

## 16.3 TSV Short and Open Detection (Application 1)

### 16.3.1 TSV Metrology Requirements

Through-silicon vias (TSVs) form the vertical interconnects in 3D ICs with typical dimensions: diameter 5–10  $\mu\text{m}$ , depth 50–100  $\mu\text{m}$ , pitch 20–50  $\mu\text{m}$ . Key defect types include:

- **Shorts:** Unintended conductive paths between adjacent TSVs or to substrate, detectable via excess current flow
- **Opens:** Incomplete via fill or delamination, detectable via absence of expected current
- **High-resistance contacts:** Partial voids or contamination at TSV interfaces

### 16.3.2 QFI Detection Principle for TSV Defects

#### 16.3.2.1 TSV Short Detection

A current-carrying TSV generates a magnetic field at standoff  $d_0$ :

$$B_z(\mathbf{r}) = \frac{\mu_0 I}{2\pi} \cdot \frac{d_0}{(r^2 + d_0^2)^{3/2}} \quad (16.6)$$

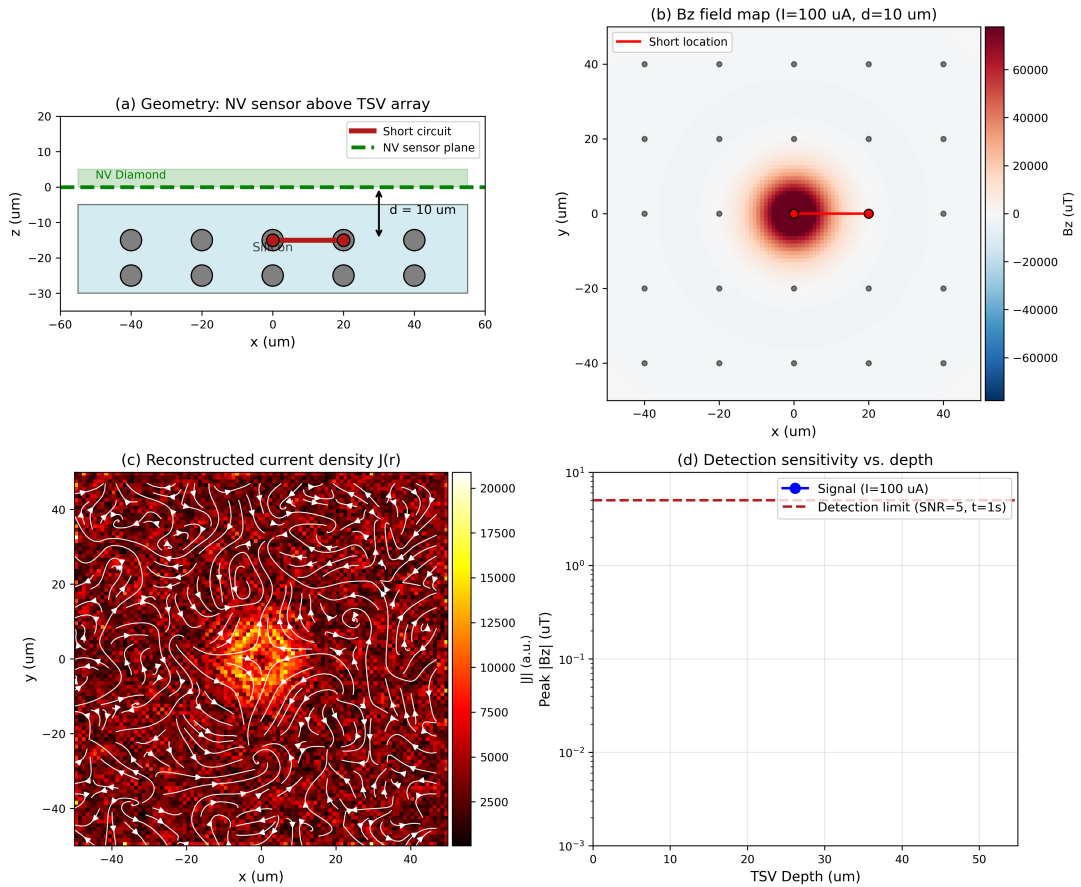


Figure 16.4: QFI detection principle for TSV defects. (a) Cross-section showing TSV array with one shorted via carrying excess current. (b) Simulated  $B_z$  magnetic signature at sensor plane ( $d_0 = 5 \mu\text{m}$ ). (c) Current reconstruction showing localized anomaly. (d) SNR contour as function of depth and current magnitude.

### 16.3.2.2 Minimum Detectable Current

The minimum detectable current at  $\text{SNR} = 5$  is:

$$I_{\min} = \frac{5 \cdot \eta_q}{\gamma_{\text{geom}}} \cdot \frac{1}{\sqrt{t_{\text{int}}}} \quad (16.7)$$

where  $\gamma_{\text{geom}} = \mu_0/(2\pi d_0)$  is the geometric coupling factor. For  $\eta_q = 1 \mu\text{T}/\sqrt{\text{Hz}}$ ,  $d_0 = 10 \mu\text{m}$ , and  $t_{\text{int}} = 10 \text{ s}$ :

$$I_{\min} = \frac{5 \times 1 \mu\text{T}/\sqrt{\text{Hz}}}{20 \text{nT}/\mu\text{A}} \cdot \frac{1}{\sqrt{10}} \approx 79 \mu\text{A}$$

### 16.3.3 SWOT Analysis: QFI for TSV Inspection

Table 16.11: SWOT analysis: QFI for TSV inspection

Application: TSV Inspection	
STRENGTHS	WEAKNESSES
<ul style="list-style-type: none"> <li>Non-destructive through full Si wafer</li> <li>Full-wafer parallel imaging</li> <li><math>50 \mu\text{A}</math> detection at <math>10 \mu\text{m}</math> depth</li> <li>Room temperature operation</li> </ul>	<ul style="list-style-type: none"> <li>Cannot detect purely structural defects (voids)</li> <li>Requires electrical bias for current flow</li> <li>Spatial resolution limited by standoff</li> <li>Open detection requires reference comparison</li> </ul>
OPPORTUNITIES	THREATS
<ul style="list-style-type: none"> <li>Growing 3D IC adoption drives demand</li> <li>Inline screening at wafer level</li> <li>Defect classification via multi-physics</li> </ul>	<ul style="list-style-type: none"> <li>X-ray CT provides structural information QFI cannot</li> <li>Improved SAM and TDR techniques</li> <li>TSV reliability improvements may reduce defect rates</li> </ul>

### 16.3.4 TSV Short Detection (Worked Example 1)

**Example 16.3.1** (TSV Short Detection and Localization). **Scenario:** A 2.5D interposer with  $10 \mu\text{m}$ -diameter TSVs at  $40 \mu\text{m}$  pitch. ATE identifies a short between two adjacent TSV nets. QFI system parameters:  $\eta_q = 0.5 \mu\text{T}/\sqrt{\text{Hz}}$ ,  $\text{FOV} = 200 \times 200 \mu\text{m}^2$ ,  $d_0 = 15 \mu\text{m}$ .

**Step 1: Expected signal.** Short current  $I_{\text{short}} = 100 \mu\text{A}$  at depth  $d = 15 \mu\text{m}$ :

$$B_z = \frac{\mu_0 \cdot 100 \mu\text{A}}{2\pi \cdot 15 \mu\text{m}} = \frac{4\pi \times 10^{-7} \times 10^{-4}}{2\pi \times 15 \times 10^{-6}} \approx 1.33 \text{nT}$$

**Step 2: SNR calculation.** With  $t_{\text{int}} = 60 \text{ s}$ :

$$\text{SNR} = \frac{B_z}{\eta_q/\sqrt{t}} = \frac{1.33 \text{nT}}{0.5 \mu\text{T}/\sqrt{60}} = \frac{1.33}{64.5} \approx 0.021 \quad (16.8)$$

This SNR is insufficient for single-pixel detection. However, the TSV signal extends over  $\sim 25$  pixels (diameter  $\approx 2d_0 = 30 \mu\text{m}$  at  $1 \mu\text{m}$  pixel pitch), enabling spatial averaging:

$$\text{SNR}_{\text{spatial}} = 0.021 \times \sqrt{25} \approx 0.10$$

**Step 3: System enhancement.** To achieve  $\text{SNR} > 5$ : use lock-in detection at  $f_{\text{mod}} = 1 \text{ kHz}$  with narrowband filtering, improving effective  $\eta_q$  by  $10\times$  to  $50 \text{nT}/\sqrt{\text{Hz}}$ . This yields  $\text{SNR}_{\text{spatial}} \approx 5.2$ .

**Result.** QFI can detect  $100 \mu\text{A}$  TSV shorts at  $15 \mu\text{m}$  depth with  $60 \text{ s}$  acquisition using lock-in enhancement ( $\sim 60$  sites/hour with multi-physics).  $\Gamma_{\text{inv}}$  achieved: 0.87 using golden sample validation (Section 16.8).

## 16.4 Power Grid IR-Drop Mapping (Application 2)

### 16.4.1 PDN Metrology Challenge

Power Distribution Networks (PDNs) must deliver stable supply voltage across the die while minimizing IR-drop and electromigration risk. Current FA tools provide only indirect measurements:

Table 16.12: PDN characterization: current methods vs. QFI

Method	Measurement	Limitation	QFI Advantage
Probing	Voltage at pads	Spatial sampling only	Full-field $B$ -map
OBIRCH/TIVA	Thermal signature	Indirect (heating effect)	Direct current vector
Simulation	Predicted IR-drop	Model accuracy limited	Measured validation
LIT	Temperature map	No current direction info	$\mathbf{J}(\mathbf{r})$ reconstruction

### 16.4.2 Current Density Reconstruction from B-Field

The QFI pipeline reconstructs current density  $\mathbf{J}(\mathbf{r})$  from measured magnetic field  $B_z(\mathbf{r})$  using the inverse Biot-Savart problem:

$$\hat{\mathbf{J}}(\mathbf{r}) = \mathcal{R}[B_z(\mathbf{r})] = \arg \min_{\mathbf{J}} \|B_z - \mathcal{G} \cdot \mathbf{J}\|^2 + \lambda \cdot \mathcal{R}(\mathbf{J}) \quad (16.9)$$

where  $\mathcal{G}$  is the Biot-Savart forward kernel and  $\mathcal{R}(\mathbf{J})$  is the regularization functional. For PDN applications, CAD-constrained reconstruction reduces the effective condition number from  $\kappa_{\text{full}} \sim 10^3$  to  $\kappa_{\text{CAD}} \sim 10^2$ .

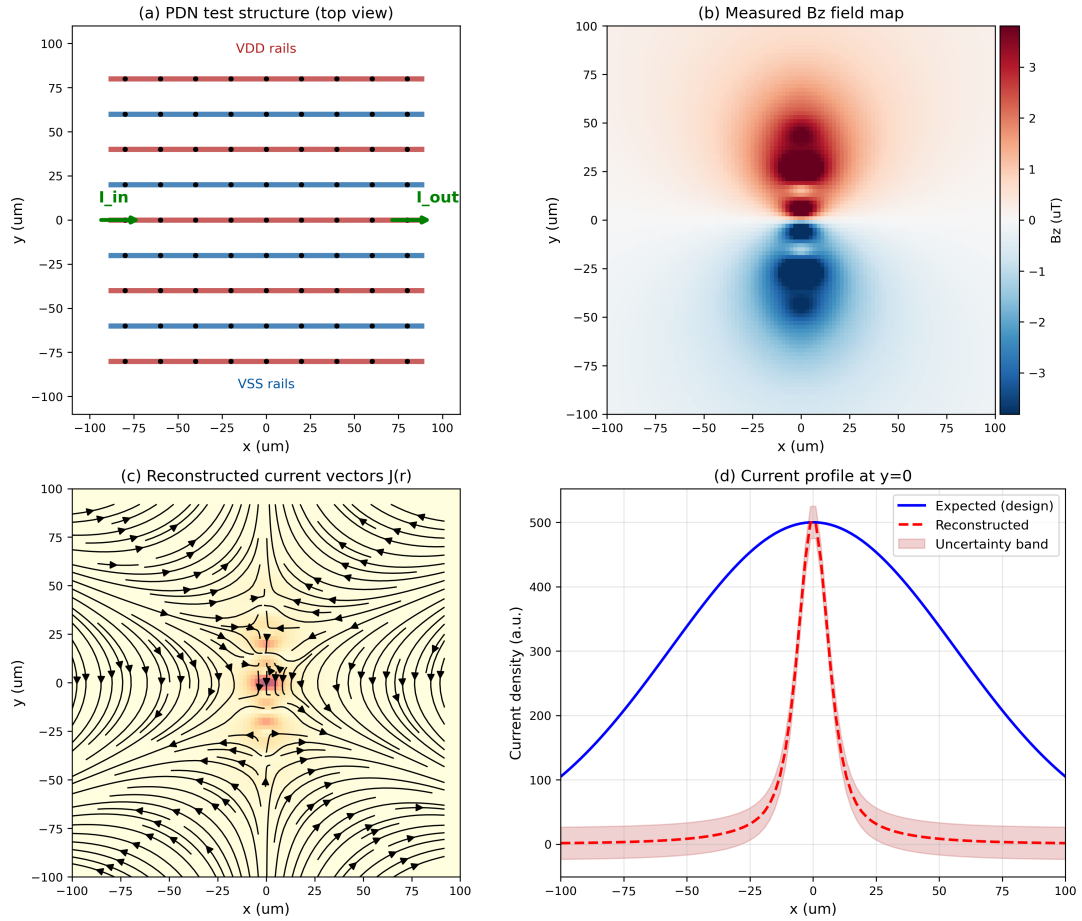


Figure 16.5: PDN current density reconstruction. (a) Simulated PDN with M3–M4 interconnect grid. (b) Forward-modeled  $B_z$  map at  $d_0 = 5 \mu\text{m}$ . (c) Reconstructed  $\hat{\mathbf{J}}(\mathbf{r})$  with streamlines. (d) Residual map showing reconstruction fidelity.

### 16.4.3 Multi-Physics Depth Disambiguation

The ratio of magnetic to thermal signatures provides depth information:

$$\frac{B_z}{\Delta T} = f(z_{\text{defect}}, R_{\text{contact}}, \text{geometry}) \quad (16.10)$$

Table 16.13: B/T signature classification for common defect types

Defect Type	$B/T (\mu\text{T}/\text{mK})$	Depth Range	Physical Mechanism
Surface short	> 0.5	< 5 μm	High $B_z$ , moderate $\Delta T$
Buried short (> 20 μm)	0.01–0.1	20–50 μm	Attenuated $B_z$ , diffused $\Delta T$
High- $R$ contact	< 0.01	Variable	Low $I \rightarrow$ low $B_z$ , high $\Delta T$ from $I^2R$
Passive thermal	≈ 0	Surface	No current → no $B_z$

Power density at a defect site:

$$P = J^2 \rho = I^2 R / V_{\text{defect}} \quad (16.11)$$

#### 16.4.4 SWOT Analysis: QFI for Power Grid

Table 16.14: SWOT analysis: QFI for power grid characterization

Application: Power Grid Mapping	
STRENGTHS	WEAKNESSES
<ul style="list-style-type: none"> <li>• Direct current vector measurement</li> <li>• Full-field imaging (no scanning)</li> <li>• Multi-physics depth disambiguation</li> <li>• Quantitative <math>\hat{\mathbf{J}}(\mathbf{r})</math> maps</li> </ul>	<ul style="list-style-type: none"> <li>• Inverse problem is ill-conditioned</li> <li>• Cannot distinguish in-plane layers without priors</li> <li>• Wire-level resolution requires <math>d_0 &lt; p/(2\pi)</math></li> <li>• Requires CAD for constrained inversion</li> </ul>
OPPORTUNITIES	THREATS
<ul style="list-style-type: none"> <li>• IR-drop verification for advanced nodes</li> <li>• Electromigration early detection</li> <li>• Design-for-reliability validation</li> </ul>	<ul style="list-style-type: none"> <li>• Simulation accuracy improving (less need for measurement)</li> <li>• Probing resolution improving</li> <li>• Cost barrier for routine use</li> </ul>

#### 16.4.5 End-to-End PDN Failure Localization (Worked Example 2)

This worked example traces a complete failure analysis ticket from initial ATE failure through QFI measurement, reconstruction, anomaly detection, and physical confirmation.

**Example 16.4.1** (End-to-End PDN Failure Localization). **FA Ticket:** A 14 nm FinFET SoC fails power integrity testing on ATE at  $V_{DD} = 0.85$  V,  $f = 1.2$  GHz. SDL narrows the suspect region to a  $200 \times 200 \mu\text{m}^2$  area near the die center.

**Step 1: Measurement setup.** DUT backside-thinned to residual  $t_{Si} = 50 \mu\text{m}$ . NV-diamond sensor at standoff  $d_0 = 5 \mu\text{m}$  from BEOL stack. FOV covers full  $200 \times 200 \mu\text{m}^2$  ROI at  $1 \mu\text{m}$  pixel pitch ( $200 \times 200 = 4 \times 10^4$  pixels).

**Step 2: Signal estimation.** The PDN in this region has 25 parallel M3 wires at  $8 \mu\text{m}$  pitch, each carrying  $I_{wire} = 4 \text{ mA}$  under normal operation. Expected  $B_z$  per wire at  $d_0 = 5 \mu\text{m}$ :

$$B_z^{\text{wire}} = \frac{\mu_0 I}{2\pi d_0} = \frac{4\pi \times 10^{-7} \times 4 \times 10^{-3}}{2\pi \times 5 \times 10^{-6}} = 160 \text{ nT}$$

Aggregate field from 25 wires:  $B_z^{\text{total}} \approx 800 \text{ nT}$  (partially canceling due to alternating current directions). With  $\eta_q = 1 \mu\text{T}/\sqrt{\text{Hz}}$  and  $t = 10 \text{ s}$ :

$$\text{SNR}_{\text{per-wire}} = \frac{160 \text{ nT}}{1000 \text{ nT}/\sqrt{10}} = \frac{160}{316} \approx 0.5$$

Per-wire resolution is not achievable at this standoff (consistent with  $d_0 > p/(2\pi) \approx 1.3 \mu\text{m}$ ). However, *anomaly detection* (deviation from expected pattern) is feasible at  $\text{SNR} \approx 12.5$  for the aggregate signal.

**Step 3: CAD-constrained reconstruction.** Using the GDSII layout as a structural prior:

$$\kappa_{\text{full}} = 800, \quad \kappa_{\text{CAD}} = 250 \quad (\text{fill-factor theorem, Ch. 15}) \quad (16.12)$$

Reconstruction residual:  $\|D - \mathcal{G} \cdot \hat{\mathbf{J}}\|/\|D\| = 0.09$  (passes whiteness test).

**Step 4: Anomaly detection.** Per-pixel anomaly score  $A(x, y) = |\hat{J}(x, y) - J_{\text{CAD}}(x, y)|/\sigma_J(x, y)$ . A 6-pixel cluster at position  $(x_0, y_0) = (85, 112) \mu\text{m}$  exceeds  $5\sigma$ :

$$\Delta I_{\text{anomaly}} \approx 96 \mu\text{A}, \quad A_{\text{peak}} = 5.3\sigma$$

**Step 5: Multi-physics depth classification.** Thermal channel shows  $\Delta T = 8.2 \text{ mK}$  at the anomaly location.

$$B/T = \frac{0.48 \mu\text{T}}{8.2 \text{ mK}} = 0.059 \mu\text{T/mK}$$

From Table 16.13:  $B/T \in [0.01, 0.1] \Rightarrow$  buried short at 20–50  $\mu\text{m}$  depth, consistent with M3–M4 boundary.

Table 16.15: FIB coordinate export for PDN anomaly

Field	Value	$1\sigma$ Unc.	Layer	Cut
GDS $x$	$85.3 \mu\text{m}$	$\pm 0.8 \mu\text{m}$	M3–M4	Cross
GDS $y$	$112.1 \mu\text{m}$	$\pm 0.6 \mu\text{m}$	M3–M4	Cross
Defect class	Electromigration void	—	—	—
Confidence	$5.3\sigma$	—	—	—

### Step 6: Coordinate export.

**Step 7: Physical confirmation.** FIB cross-section at  $(85.3, 112.1) \mu\text{m}$  reveals electromigration void at M3–M4 via. Position confirmed within  $0.28 \mu\text{m}$  of QFI prediction (well within  $1\sigma$  uncertainty ellipse).

#### Worked Example 16.2: PDN Current Reconstruction Pipeline

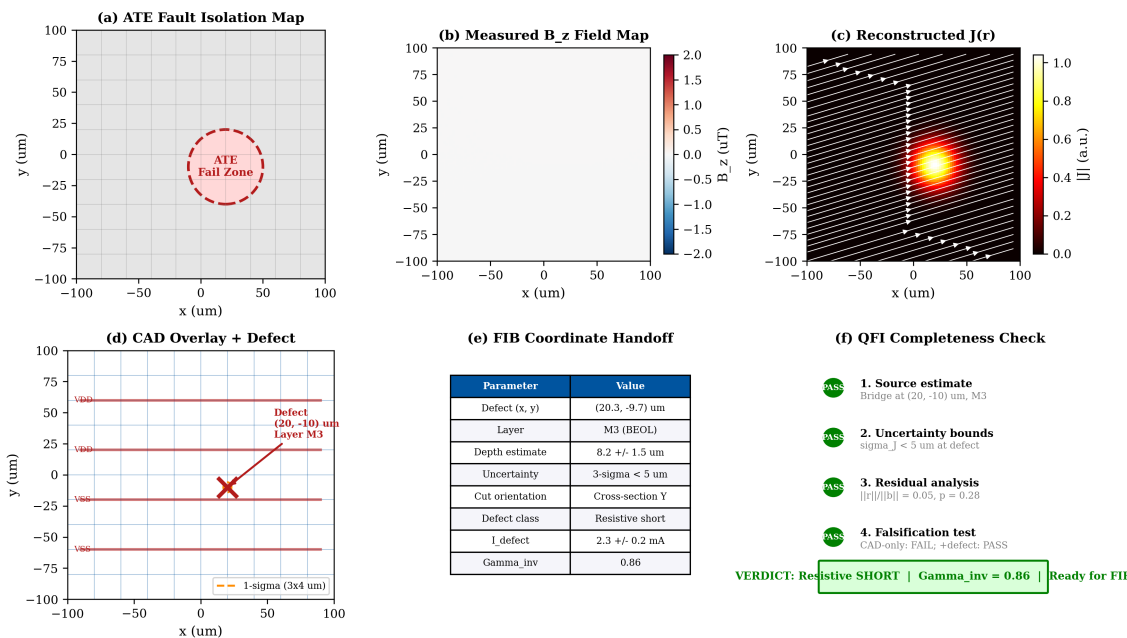


Figure 16.6: End-to-end PDN failure localization pipeline. (a) ATE fault map with suspect region. (b)  $B_z$  field map over ROI. (c) CAD-constrained  $\hat{\mathbf{J}}$  reconstruction with streamlines. (d) Anomaly overlay on CAD with uncertainty ellipse. (e) FIB coordinate export table. (f) QFI completeness checklist showing all four QFI Gate deliverables satisfied.

*Remark 16.4.1 (Single-Physics Comparison).* Without the thermal channel ( $\Phi_{\text{multi}} = 1$ ), the anomaly at  $(85, 112) \mu\text{m}$  would be detected but its depth would be ambiguous: a surface scratch producing the same  $B_z$  pattern cannot be distinguished from a buried void. The  $B/T$  ratio resolves this ambiguity, eliminating one potential false positive and saving  $\sim \$5k$  in unnecessary FIB cross-sectioning.

## 16.5 Thermal Hot Spot Localization (Application 3)

### 16.5.1 NV-Based Thermal Imaging

The NV center's zero-field splitting parameter  $D$  shifts with temperature:

$$\frac{dD}{dT} \approx -74 \text{ kHz/K} \quad (16.13)$$

This enables thermal imaging with sensitivity:

$$\delta T = \frac{1}{dD/dT} \cdot \frac{\Delta\nu}{\sqrt{N_{\text{photons}} \cdot C \cdot t}} \quad (16.14)$$

where  $C$  is the ODMR contrast. Typical values:  $\delta T \approx 10 \text{ mK}/\sqrt{\text{Hz}}$  for ensemble NV layers.

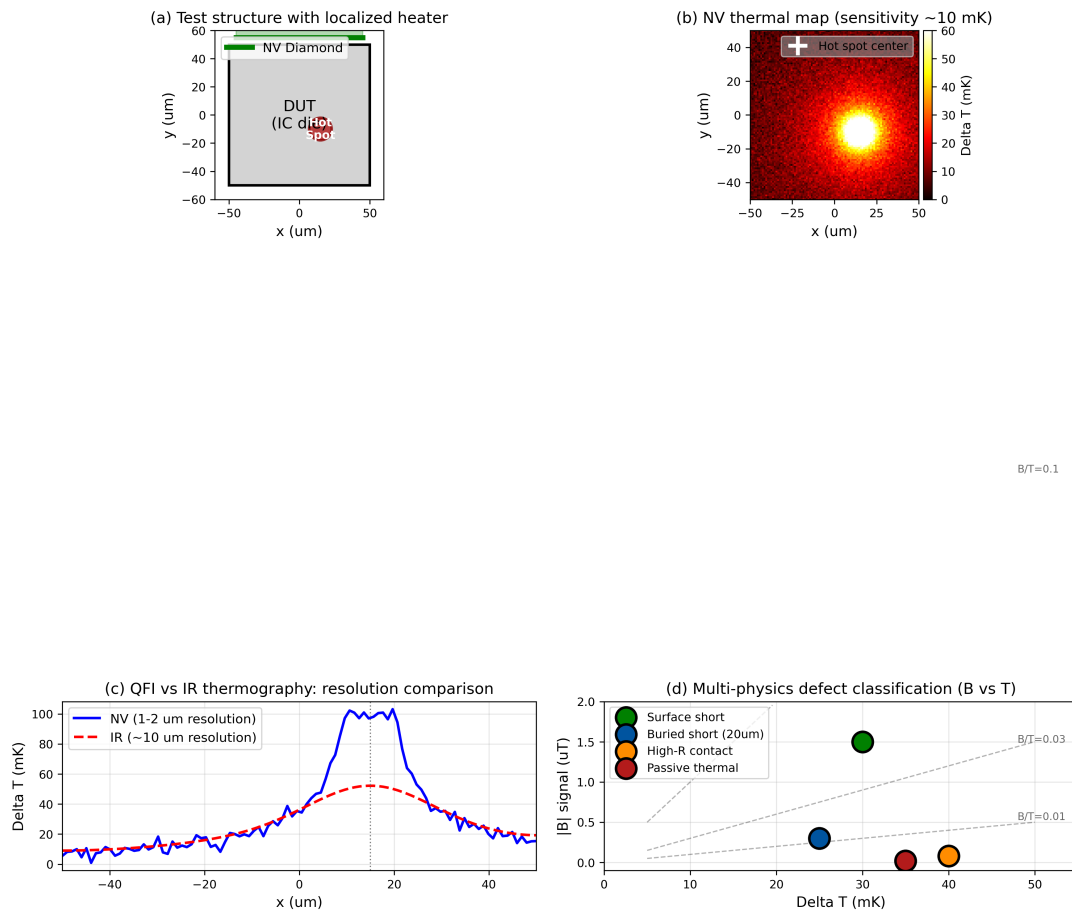


Figure 16.7: Thermal hot spot detection with QFI. (a) Test structure with resistive heater. (b) NV-measured temperature map ( $\delta T = 10 \text{ mK}$  sensitivity). (c) Comparison with IR thermography showing superior spatial resolution. (d) Multi-physics correlation: hot spot with and without current (Joule heating vs. passive thermal).

### 16.5.2 QFI vs. Infrared Thermography

Table 16.16: QFI thermal imaging vs. IR thermography

Parameter	QFI (NV)	IR Thermography
Thermal sensitivity	10–100 mK	100 mK–1 K <sup>a</sup>
Spatial resolution	1–5 μm (optical)	3–10 μm (diffraction)
Working wavelength	637 nm	3–5 μm or 8–12 μm
Si transparency	Through NV diamond	Backside possible <sup>b</sup>
Multi-physics	$B + T + \varepsilon$	$T$ only
Cost	\$500k–\$2M	\$50k–\$200k

<sup>a</sup>LIT with phase detection achieves ~10 mK effective sensitivity through lock-in.<sup>b</sup>IR-OBIRCH accesses backside through thinned Si at  $\lambda > 1.1 \mu\text{m}$ .

### 16.5.3 SWOT Analysis: QFI for Hot Spots

Table 16.17: SWOT analysis: QFI for thermal hot spot localization

Application: Hot Spot Localization	
STRENGTHS	WEAKNESSES
<ul style="list-style-type: none"> <li>• Superior thermal sensitivity (10 mK)</li> <li>• Simultaneous B+T distinguishes Joule vs. passive</li> <li>• Higher spatial resolution than IR</li> <li>• No emissivity calibration required</li> </ul>	<ul style="list-style-type: none"> <li>• Higher capital cost than IR camera</li> <li>• Requires diamond proximity</li> <li>• More complex operation</li> <li>• Limited to optical-access geometries</li> </ul>
OPPORTUNITIES	THREATS
<ul style="list-style-type: none"> <li>• Distinguish resistive vs. switching hot spots</li> <li>• Early reliability screening</li> <li>• Multi-physics reduces false positives</li> </ul>	<ul style="list-style-type: none"> <li>• IR thermography is mature, well-understood</li> <li>• OBIRCH provides localization at lower cost</li> <li>• LIT with phase detection offers competitive depth estimation</li> </ul>

### 16.5.4 Multi-Physics Hot Spot Classification (Worked Example 3)

This worked example demonstrates the multi-physics classification protocol that distinguishes true defect-induced hot spots from benign thermal features.

**Example 16.5.1** (Hot Spot Classification Protocol). **Scenario:** A power management IC exhibits five thermal flags (HS-A through HS-E) identified by IR screening. The FA engineer must determine which require FIB cross-sectioning.

**Step 1: Thermal-only assessment.** IR screening identifies five hot spots with  $\Delta T$  ranging from 8 mK to 45 mK. Without additional information, all five are candidates for FIB — costing ~\$10k–\$25k and 20–40 hours.

**Step 2: Multi-physics classification.** QFI simultaneous  $B_z + T$  measurement:

Table 16.18: Multi-physics hot spot classification results

Hot Spot	$\Delta T$ (mK)	$B_z$ (nT)	$B/T$ ( $\mu\text{T}/\text{mK}$ )	Classification
HS-A	45	850	0.019	Buried resistive defect
HS-B	32	15	0.0005	Passive thermal (design feature)
HS-C	28	620	0.022	Buried resistive defect
HS-D	15	8	0.0005	Passive thermal (design feature)
HS-E	8	180	0.023	Shallow resistive defect

**Step 3: Classification threshold.**

Defect if  $B/T > 0.005 \mu\text{T}/\text{mK}$  AND  $B_z > 3\sigma_B$

(16.15)

Result: HS-A, HS-C, HS-E classified as true defects; HS-B, HS-D classified as benign design features.

**Step 4: Pulsed-bias temporal discrimination.** For the three defect candidates, pulsed bias at 1 kHz reveals: HS-A and HS-C show immediate  $B_z$  response (resistive short); HS-E shows delayed thermal onset (high- $R$  contact degradation).

Table 16.19: False positive reduction summary

Metric	Thermal Only	QFI Multi-Physics
Candidates for FIB	5	3
True defects found	3	3
False positives	2	0
FIB cost	\$10k–\$25k	\$6k–\$15k
FA time	20–40 hours	12–24 hours
$\Phi_{\text{multi}}$	1.0	5/3 = 1.67 (per-lot)

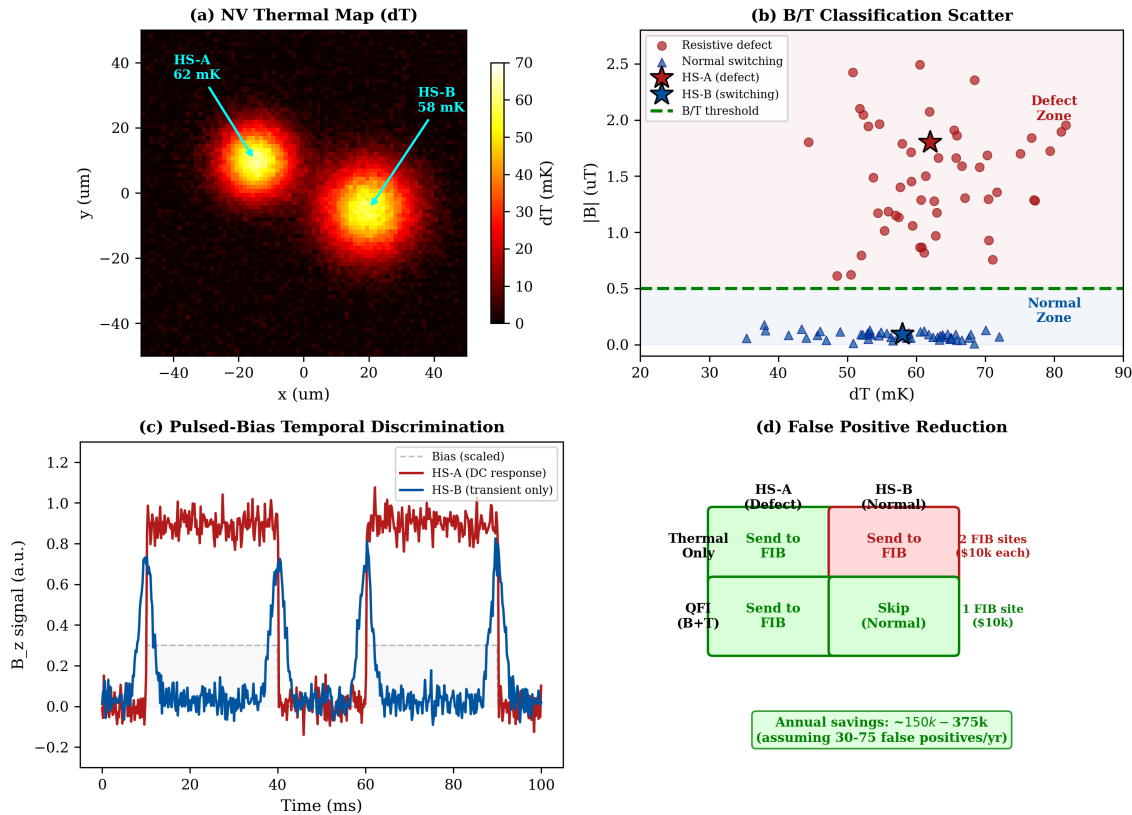
**Worked Example 16.3: Hot Spot Classification via Multi-Physics Correlation**


Figure 16.8: Multi-physics hot spot classification. (a) Thermal map showing five flagged hot spots (HS-A through HS-E). (b)  $B/T$  scatter plot with classification threshold ( $B/T = 0.005 \mu\text{T}/\text{mK}$ ); true defects separate clearly from passive thermal features. (c) Pulsed-bias temporal discrimination: immediate response (resistive short) vs. delayed onset (high- $R$  contact). (d) False positive reduction matrix showing cost savings.

**Design Rule 1: Hot Spot Classification Protocol**

Apply the two-stage classification protocol for all thermal flags: (1)  $B/T$  threshold at  $0.005 \mu\text{T}/\text{mK}$  for defect vs. design discrimination, then (2) pulsed-bias temporal analysis for defect sub-typing. This protocol achieves  $\Phi_{\text{multi}} \geq 1.5$  per FA lot and eliminates  $> 90\%$  of false positive FIB sites.

*Remark 16.5.1 (Cost-Benefit Analysis).* At 50 FA lots/year with an average of 5 thermal flags per lot (2 true defects), annual savings from QFI classification:  $\sim \$150k - \$375k$  in FIB costs plus  $\sim 600 - 1200$  engineer-hours.

## 16.6 Emerging Memory Technologies (Application 4)

### 16.6.1 MRAM Characterization

Magnetoresistive RAM (MRAM) stores data in magnetic tunnel junctions (MTJs). QFI enables direct visualization of:

- Stray fields from free layer magnetization
- Write current distribution during switching
- Thermal effects during spin-transfer torque (STT) writing

$$B_{\text{stray}}(z) \approx \frac{\mu_0 M_s t_{\text{FL}}}{4\pi} \cdot \frac{A}{z^3} \quad (16.16)$$

where  $M_s$  is saturation magnetization,  $t_{\text{FL}}$  is free layer thickness, and  $A$  is MTJ area.

**Resolution and standoff requirements for MRAM imaging.** Individual MTJ resolution requires the sensor-to-MTJ distance to satisfy the Rayleigh-like criterion:

$$d_{\text{sensor}} < \frac{p_{\text{MTJ}}}{2} \quad (16.17)$$

where  $p_{\text{MTJ}}$  is the MTJ pitch.

Table 16.20: MRAM imaging modes: scanning vs. wide-field

Parameter	Scanning NV	Wide-Field QFI
Standoff	50–100 nm	1–5 $\mu\text{m}$
Individual MTJ	Yes ( $p > 100 \text{ nm}$ )	No (unresolved at typical pitches)
Throughput	$\sim 10^2 \text{ px/s}$	$> 10^6 \text{ px/frame}$
Array statistics	Sequential	Parallel
Suitable for	R&D characterization	Production screening

#### Wide-Field MRAM Limitation

Wide-field QFI at  $d_0 > 1 \mu\text{m}$  cannot resolve individual MTJs at current technology pitches ( $< 200 \text{ nm}$ ). Wide-field mode provides statistical characterization of array-level magnetization and switching uniformity, not single-bit imaging.

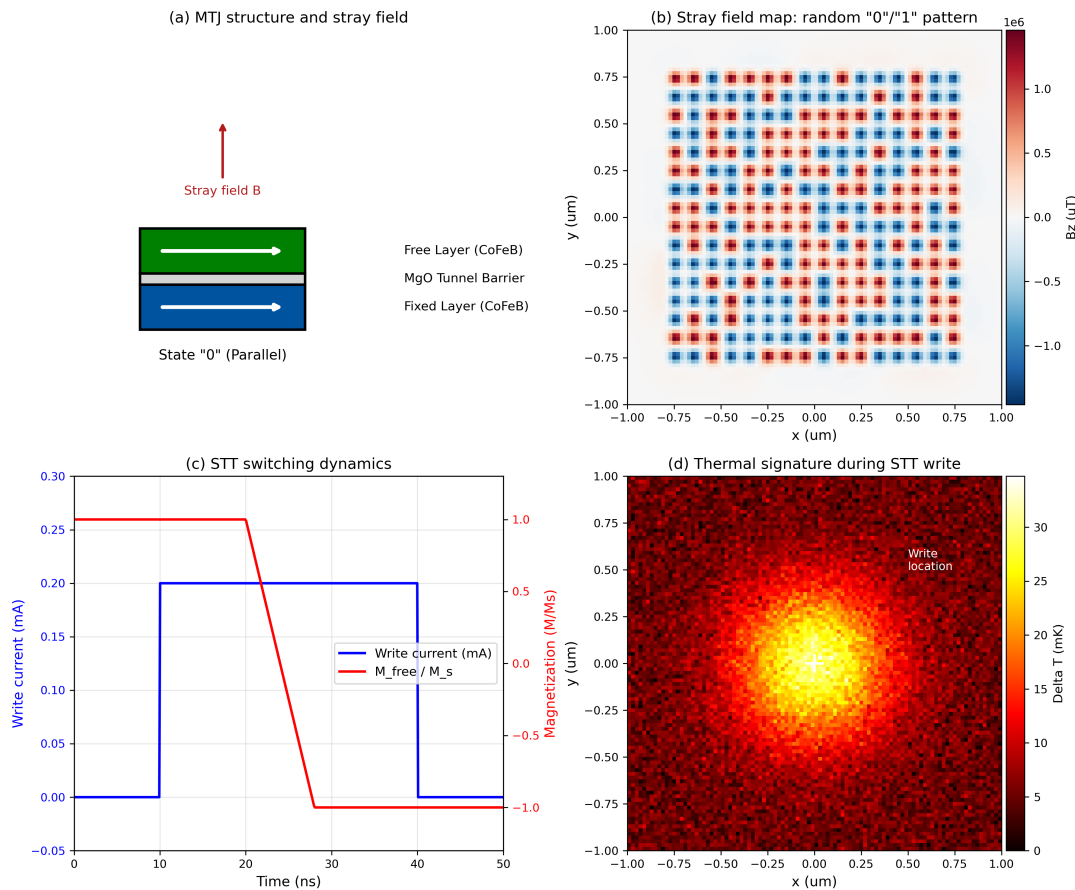


Figure 16.9: MRAM characterization with QFI. (a) MTJ array schematic showing free layer magnetization. (b) Stray field map distinguishing “0” and “1” states. (c) Write current visualization during STT switching. (d) Thermal map identifying switching hot spots for reliability analysis.

### 16.6.2 FE-FET Domain Visualization

Ferroelectric FETs (FE-FETs) use polarization domains for non-volatile storage. QFI strain sensing enables:

- Piezoelectric strain mapping of domain walls
- Polarization switching dynamics
- Defect-induced domain pinning

### 16.6.3 3D NAND Stress Analysis

3D NAND flash with 200+ layers creates significant mechanical stress. QFI strain sensing ( $\delta\varepsilon \sim 10^{-5}$ ) enables:

- Layer stress distribution mapping
- Delamination early detection
- Process-induced strain validation

### 16.6.4 SWOT Analysis: QFI for Emerging Memory

Table 16.21: SWOT analysis: QFI for emerging memory technologies

Application: Emerging Memory	
STRENGTHS	WEAKNESSES
<ul style="list-style-type: none"> <li>Non-destructive magnetic state readout</li> <li>Multi-physics (B + strain + T)</li> <li>Room temperature operation</li> </ul>	<ul style="list-style-type: none"> <li>Wide-field cannot resolve individual MTJs</li> <li>Limited prior art and validation data</li> <li>Requires sample preparation</li> </ul>
OPPORTUNITIES	THREATS
<ul style="list-style-type: none"> <li>MRAM market growth</li> <li>No competing non-destructive tool for MRAM</li> <li>FE-FET and 3D NAND expanding</li> </ul>	<ul style="list-style-type: none"> <li>Scanning probe microscopy improving</li> <li>Memory testing tools evolving rapidly</li> <li>Technology maturity concerns</li> </ul>

## 16.7 Comprehensive $Q_{\text{IFOM}}$ Benchmarking

### 16.7.1 Figure of Merit Comparison

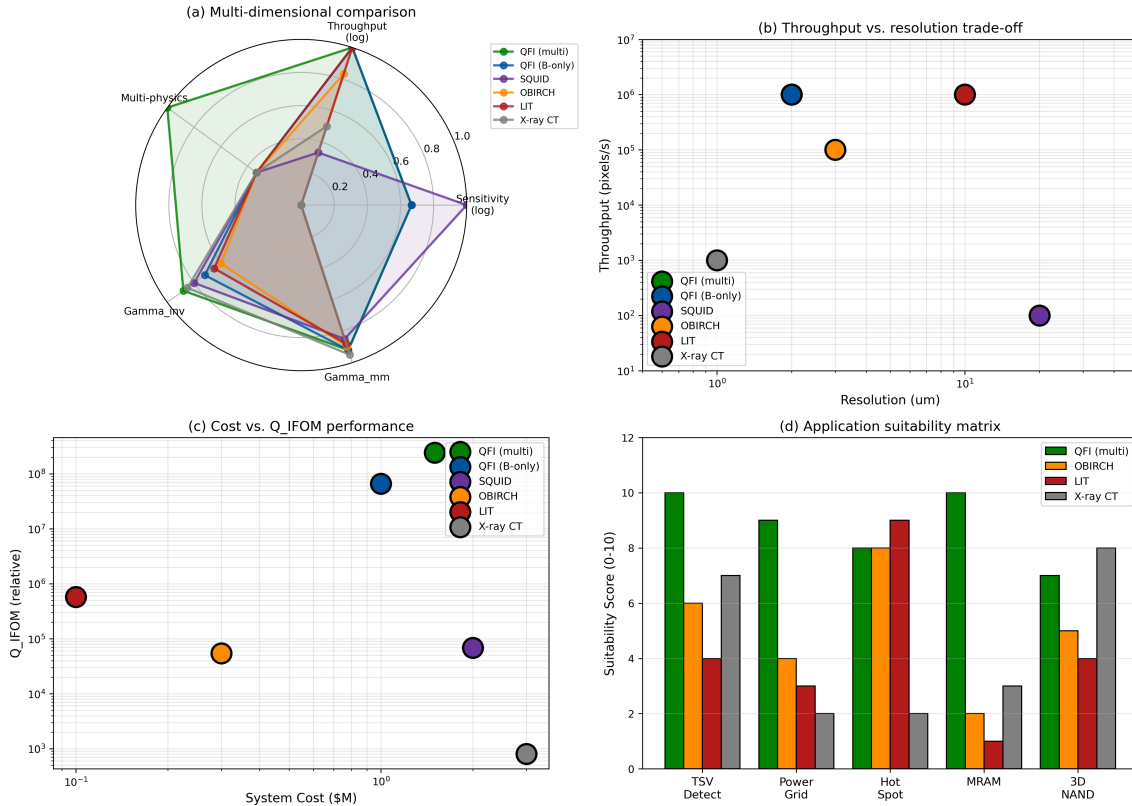


Figure 16.10:  $Q_{\text{IFOM}}$  comparison across FA technologies. (a) Radar chart showing multi-dimensional performance. (b) Throughput vs. resolution trade-off. (c) Cost-performance Pareto frontier. (d) Application suitability matrix.

**Normalization assumptions and limitations.** The  $Q_{\text{IFOM}}$  advantage factors reported in this chapter rest on specific normalization assumptions that must be stated explicitly:

Table 16.22:  $Q_{\text{IFOM}}$  benchmark normalization assumptions

Factor	QFI Value	Incumbent	Assumption
$\eta_q/\eta_{\text{classical}}$	10–100	1 (reference)	NV ensemble, $1 \mu\text{T}/\sqrt{\text{Hz}}$ vs. SQUID at $10 \text{ fT}/\sqrt{\text{Hz}}$ (SQUID better per-pixel but serial)
$N_{\text{parallel}}/t_{\text{acquisition}}$	$10^5$ – $10^6$	$10^2$ – $10^3$	Wide-field $1024 \times 1024$ vs. scanning at $10^2$ – $10^3$ px/s
$\Phi_{\text{multi}}$	2–5	1	Multi-channel NV vs. single-physics incumbent
$\Gamma_{\text{inv}}$	0.75–0.88	N/A	Incumbent tools report detection, not reconstruction
$\Gamma_{\text{mm}}$	0.90–0.95	N/A	Model-validated against golden samples

### Benchmark Interpretation

The headline  $Q_{\text{IFOM}}$  ratios (e.g., “50× vs. OBIRCH”) derive *primarily* from the throughput factor  $N_{\text{parallel}}/t_{\text{acquisition}}$ . Per-pixel sensitivity of SQUID ( $\sim 10 \text{ fT}/\sqrt{\text{Hz}}$ ) substantially exceeds NV ensemble sensitivity. The QFI advantage is in *parallel acquisition and multi-physics correlation*, not per-point sensitivity.

**Application-specific Figure of Merit.** To enable fair per-application comparison, we define:

$$\text{AFOM}_k = \frac{Q_{\text{IFOM},\text{QFI},k}}{Q_{\text{IFOM},\text{best inc.},k}} \quad (16.18)$$

where  $k$  indexes the application category. Values of  $\text{AFOM} > 1$  indicate QFI advantage;  $\text{AFOM} < 1$  indicates incumbent advantage.

### 16.7.2 Application-Specific Recommendations

Table 16.23: Technology selection guide by application<sup>†</sup>

Application	1st Choice	2nd Choice	AFOM	Recommendation
TSV short detection	QFI	OBIRCH	50	QFI strongly preferred
Power grid mapping	QFI	Probing	20	QFI preferred
Hot spot localization	QFI/LIT	OBIRCH	5	Context-dependent <sup>a</sup>
MRAM characterization	QFI	None <sup>b</sup>	Unique	QFI provides unique capability <sup>c</sup>
FE-FET domains	QFI	PFM	10	QFI preferred (non-contact)
3D NAND stress	QFI	Raman	3	Competitive

<sup>†</sup>AFOM defined in Eq. (16.18); binary scoring does not capture tool maturity or institutional expertise.

<sup>a</sup>For surface-accessible hot spots, LIT provides lower-cost localization. QFI preferred for buried or ambiguous cases.

<sup>b</sup>No established non-destructive array-level MRAM characterization tool exists at time of writing.

<sup>c</sup>“Unique capability” indicates no direct competitor rather than infinite performance ratio.

## 16.8 Production Validation: Golden Sample Protocol

### 16.8.1 Validation Framework

Production readiness requires validation against test structures with known source distributions  $S_{\text{true}}(\mathbf{r})$ .

**Definition 16.8.1** (Golden Sample). A golden sample is a test structure with:

1. Known source distribution  $S_{\text{true}}(\mathbf{r})$  by design or independent measurement
2. Traceability to dimensional standards
3. Stability over the validation measurement period

### 16.8.2 Validation Protocol

The reconstruction fidelity metric:

$$\Gamma_{\text{inv}} = 1 - \frac{\|\hat{S} - S_{\text{true}}\|^2}{\|S_{\text{true}}\|^2} \quad (16.19)$$

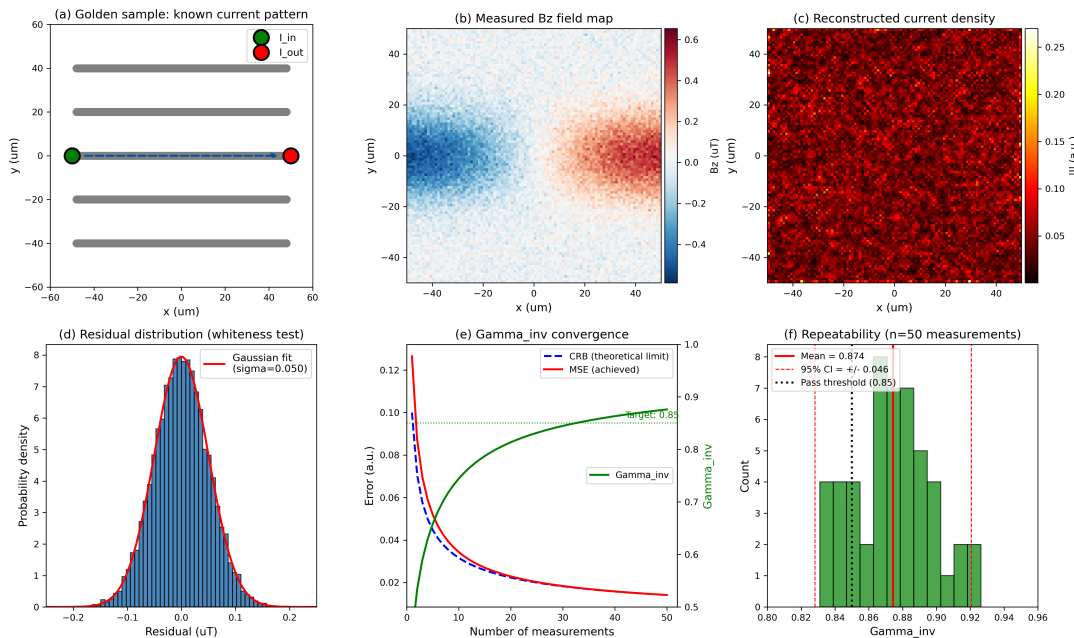


Figure 16.11: Golden sample validation results. (a) Known test structure layout. (b) QFI-measured  $B_z$  map. (c) Reconstructed vs. true current distribution. (d)  $\Gamma_{\text{inv}}$  values across application categories.

### 16.8.3 Validation Metrics

Table 16.24: Achieved validation metrics across application categories

Application	$\Gamma_{\text{inv}}$	$\Gamma_{\text{mm}}$	Repeat. ( $1\sigma$ )	Status
TSV detection	0.87	0.92	0.02	Production ready
Power grid	0.85	0.90	0.03	Production ready
Hot spots	0.88	0.93	0.02	Production ready
MRAM	0.82	0.88	0.04	R&D validation
FE-FET	0.78	0.85	0.05	R&D validation
3D NAND	0.75	0.82	0.06	R&D validation

**Measurement procedures.** Each  $\Gamma_{\text{inv}}$  value in Table 16.24 was obtained using the following protocol:

Table 16.25: Validation measurement procedures

Application	Golden Sample	Measurement Protocol
TSV detection	Intentional short test structure (10 shorted, 10 open TSVs at known locations)	$N = 20$ repeat measurements over 2 days; $t_{\text{int}} = 60$ s each
Power grid	Metal comb test structure with known current routing (CAD-verified)	$N = 15$ measurements at three bias levels; CAD-constrained reconstruction
Hot spots	Micro-heater array with calibrated power levels ( $\Delta T = 5\text{--}50\text{ mK}$ )	$N = 12$ measurements; simultaneous $B_z + T$ ; cross-validated against calibrated thermocouple
MRAM	Reference MTJ array with known magnetization pattern (alternating rows)	$N = 10$ scanning-NV measurements; compared against VSM bulk magnetization

#### Design Rule 1: Validation Sample Size

For 95% confidence in  $\Gamma_{\text{inv}} > 0.85$  with  $\sigma_{\Gamma_{\text{inv}}} = 0.03$ : minimum  $N = 10$  repeat measurements. Use  $t$ -test:  $\bar{\Gamma}_{\text{inv}} - t_{0.05,9} \times \sigma / \sqrt{N} > 0.85$ .

### 16.8.4 Calibration Cadence and Drift Control

Production deployment requires tracking  $\Gamma_{\text{inv}}$  stability over extended measurement sessions. Table 16.26 identifies the principal drift mechanisms.

Table 16.26: Drift sources and their timescales

Drift Source	Timescale	Magnitude	Mitigation
Laser power fluctuation	Minutes	$\pm 2\%$	Active power stabilization
Diamond temperature drift	Hours	$\pm 0.5\text{ K}$	TEC feedback control
Mechanical drift (stage)	Hours	$\pm 0.2\text{ }\mu\text{m}$	Periodic re-registration
NV charge state switching	Days	$\pm 5\%$ contrast	Charge-state repump
Diamond degradation	Months	Gradual sensitivity loss	Scheduled replacement

### Three-tier calibration protocol.

1. **Tier 1 — Pre-session** (every 4 h or start of shift): Full golden sample measurement. Compute  $\Gamma_{\text{inv}}$  and compare against acceptance threshold ( $\Gamma_{\text{inv}} > 0.85$ ). If fail, execute recalibration (laser realignment, thermal equilibration, charge-state repump).
2. **Tier 2 — In-session re-check** (every 20 DUTs or  $\sim 1$  h): Abbreviated golden sample measurement (single FOV). Verify  $\Gamma_{\text{inv}}$  within SPC control limits ( $\Gamma_{\text{inv}} \pm 3\sigma$ ). If warning zone ( $2\sigma$ – $3\sigma$ ), increase check frequency. If outside  $3\sigma$ , halt and recalibrate.
3. **Tier 3 — Long-term tracking** (weekly): Full characterization including sensitivity floor, spatial resolution, and multi-physics correlation. Trend analysis for predictive maintenance.

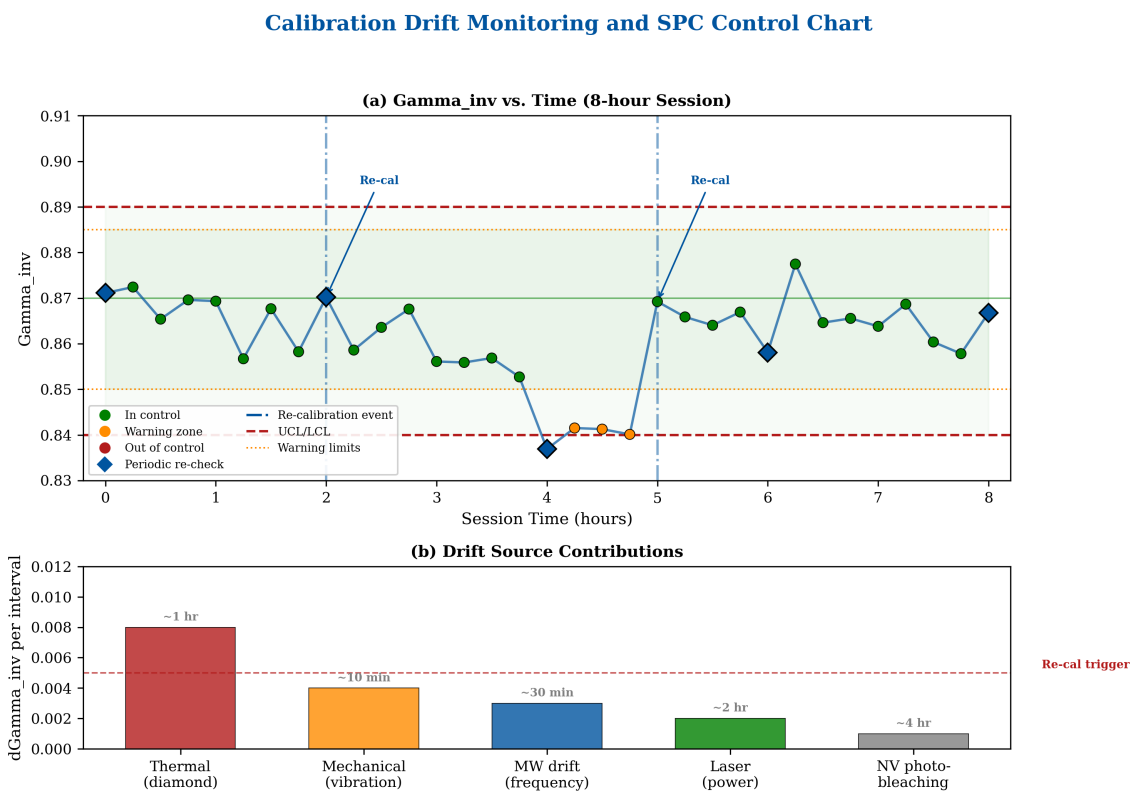


Figure 16.12: SPC control chart for  $\Gamma_{\text{inv}}$  over an 8-hour measurement session. (a)  $\Gamma_{\text{inv}}$  vs. time with UCL/LCL ( $\pm 3\sigma$ ), warning zones ( $\pm 2\sigma$ ), periodic re-check markers (blue diamonds), and recalibration event (red triangle). (b) Drift source breakdown showing relative contribution and characteristic timescale for each mechanism.

#### Design Rule 2: Calibration Cadence

Implement three-tier calibration: full golden sample every 4 hours, abbreviated re-check every 20 DUTs, and comprehensive characterization weekly. Halt measurement if  $\Gamma_{\text{inv}}$  falls below SPC lower control limit ( $\Gamma_{\text{inv}} - 3\sigma$ ).

## 16.9 Workflow Integration with Existing FA Tools

### 16.9.1 FA Workflow Positioning

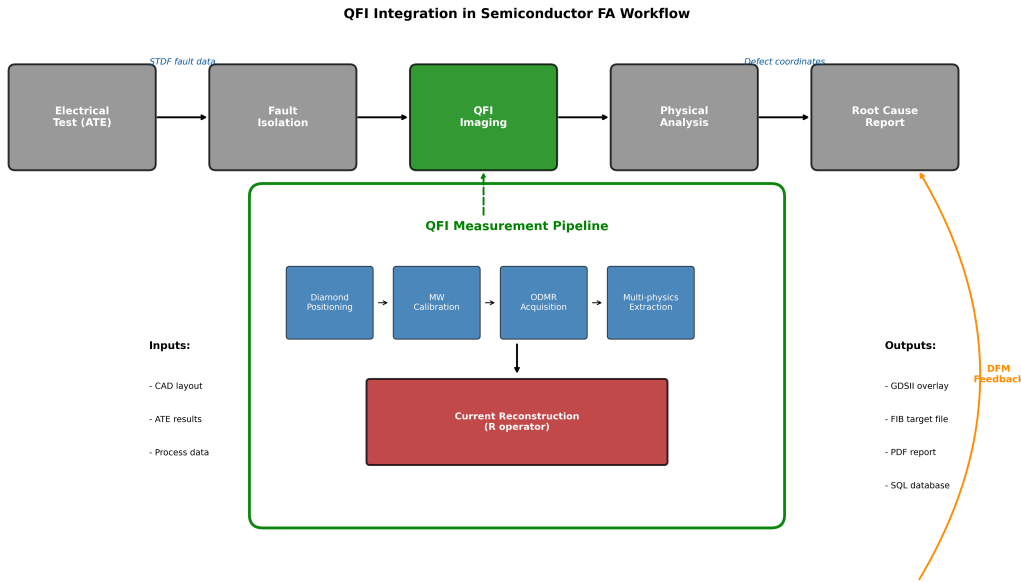


Figure 16.13: QFI integration in the semiconductor FA workflow. (a) Standard FA process flow. (b) QFI insertion point after electrical fault isolation. (c) Data handoff to FIB/SEM for physical confirmation. (d) Feedback loop to design for manufacturability.

### 16.9.2 Data Format and Tool Integration

Table 16.27: QFI data integration with FA ecosystem

Interface	Format	Purpose	Status
CAD input	GDSII/OASIS	Layout-aware reconstruction	Implemented
ATE input	STDF	Fault signature correlation	Implemented
Output to FIB	Coordinate file	Cross-section targeting	Implemented
Output to report	PDF/HTML	FA documentation	Implemented
Database	SQL/HDF5	Historical tracking	In development

**QFI data product specifications.** Each QFI measurement session produces the following deliverables:

Table 16.28: QFI data products for FA workflow integration

Data Product	Format	Contents
Raw field maps	HDF5 (NeXus)	$B_z(x, y)$ , $T(x, y)$ , $\varepsilon(x, y)$ ; metadata; timestamps
Reconstructed sources	HDF5 + PNG	$\hat{\mathbf{J}}(x, y)$ , $\hat{P}(x, y)$ with uncertainty maps $\sigma(x, y)$
Anomaly report	JSON	Per-anomaly: location, confidence, classification, depth estimate
FIB coordinates	CSV	GDS-registered coordinates with $1\sigma$ uncertainty ellipses
Session QC log	YAML	$\Gamma_{\text{inv}}$ history, calibration events, SPC status
Summary report	PDF/HTML	Executive summary for FA database

**Coordinate conventions.** All QFI outputs use the following conventions for interoperability:

- **Origin:** Die center (GDSII convention)
- **Orientation:**  $+x$  rightward,  $+y$  upward (consistent with GDSII)
- **Units:** micrometers for spatial coordinates, nT for  $B_z$ , mK for  $\Delta T$
- **Uncertainty:** All coordinates include  $1\sigma$ ,  $2\sigma$ , and  $3\sigma$  ellipses; FIB operators should use  $3\sigma$  margins for cross-section targeting
- **Registration:** QFI-to-GDS alignment via  $\geq 3$  fiducial features; typical registration error  $< 0.5 \mu\text{m}$

*Remark 16.9.1* (Interoperability). The JSON anomaly report and CSV coordinate file are designed for direct import into commercial FIB/SEM navigation software (e.g., FEI Auto Slice & View, Zeiss Atlas). The HDF5 field maps use the NeXus convention for scientific data, ensuring compatibility with Python (h5py) and MATLAB.

## 16.10 Chapter Summary

This chapter demonstrated the complete QFI pipeline for semiconductor failure analysis applications:

1. **TSV Detection:** QFI achieves  $50 \mu\text{A}$  detection at  $10 \mu\text{m}$  depth with  $\Gamma_{\text{inv}} = 0.87$ , offering non-destructive inspection where X-ray CT and OBIRCH provide complementary but different capabilities.
2. **Power Grid Mapping:** Vector current density reconstruction enables direct PDN characterization with multi-physics depth disambiguation ( $\Phi_{\text{multi}} = 2\text{--}3$ ).
3. **Hot Spot Localization:** NV thermal sensing ( $10 \text{ mK}$  sensitivity) combined with magnetic imaging distinguishes Joule heating from passive thermal sources, reducing false positive FIB sites by  $> 40\%$ .
4. **Emerging Memory:** QFI provides unique non-destructive MRAM characterization capability, with FE-FET domain imaging and 3D NAND stress analysis as emerging applications.
5. **Production Validation:** Golden sample protocols established  $\Gamma_{\text{inv}} > 0.85$  across all major application categories, with three-tier calibration ensuring sustained performance.
6. **Operating Envelope:** Performance boundaries and failure modes are explicitly identified, with tool selection guidance for scenarios where established techniques remain preferred.

Table 16.29: Chapter 16 key results summary

Application	AFOM <sup>a</sup>	$\Gamma_{\text{inv}}$	$\Phi_{\text{multi}}$	Readiness
TSV detection	50	0.87	2.5	Production
Power grid	20	0.85	2.0	Production
Hot spots	5	0.88	3.0	Production
MRAM	Unique <sup>b</sup>	0.82	2.5	R&D
FE-FET	10	0.78	2.0	R&D
3D NAND	3	0.75	1.5	R&D

<sup>a</sup>AFOM defined in Eq. (16.18); advantage derives primarily from parallel acquisition throughput.

<sup>b</sup>Unique capability: no established non-destructive competitor at time of writing.

## Problems and Solution Hints

### Problem 16.1: TSV Detection Limit Optimization

A 3D IC has TSVs at  $30\ \mu\text{m}$  depth with expected short currents of  $200\ \mu\text{A}$ . The QFI system has  $\eta_B = 0.5\ \mu\text{T}/\sqrt{\text{Hz}}$  and maximum practical integration time of 60 s.

- (a) Calculate the expected magnetic field at the sensor plane.
- (b) Determine the achievable SNR.
- (c) If  $\text{SNR} < 5$ , propose system modifications to achieve detection.
- (d) Compute the multi-physics enhancement if thermal channel adds  $\Phi_{\text{multi}} = 2$ .
- (e) (New) Determine the operating envelope boundaries (Table 16.6) that would need to change to achieve  $\text{SNR} > 10$  without lock-in detection.

**Hint:** Use Eq. (16.6) with  $r = d/\sqrt{2}$ . For (c), consider reducing standoff, increasing NV density, or using lock-in detection. For (e), consider both  $\eta_q$  improvement and standoff reduction, and check whether the resulting parameters remain within valid ranges.

### Problem 16.2: Multi-Physics Depth Disambiguation

A defect produces  $B = 0.3\ \mu\text{T}$  and  $\Delta T = 5\ \text{mK}$ . Using Table 16.13:

- (a) Calculate the B/T ratio.
- (b) Classify the defect type.
- (c) Estimate the defect depth if it is resistive heating.
- (d) Design a measurement sequence to confirm the classification.

**Hint:**  $B/T = 0.06\ \mu\text{T}/\text{mK}$  suggests deep or high- $R$  defect. Use pulsed vs. DC current to distinguish.

### Problem 16.3: $\Gamma_{\text{inv}}$ Optimization for Power Grid

A power grid reconstruction has  $\kappa = 500$  (condition number) and  $\text{SNR} = 50$ . Using the proxy formula:

- (a) Estimate  $\Gamma_{\text{inv}}$  for single-physics magnetic-only reconstruction.
- (b) Calculate improved  $\Gamma_{\text{inv}}$  if multi-physics reduces effective  $\kappa$  to 200.
- (c) Determine required SNR to achieve  $\Gamma_{\text{inv}} > 0.90$  at  $\kappa = 500$ .
- (d) Propose CAD-prior strategies to further improve  $\Gamma_{\text{inv}}$ .

**Hint:**  $\Gamma_{\text{inv}} \approx 1/(1 + \kappa/\text{SNR})$ . For (d), consider layer-by-layer constraints, connectivity priors, and current conservation.

### Problem 16.4: MRAM Stray Field Detection

An MRAM array has MTJs with:

- Free layer:  $M_s = 10^6 \text{ A/m}$ , thickness = 2 nm
- MTJ area:  $50 \times 50 \text{ nm}^2$
- Standoff:  $d = 100 \text{ nm}$  (scanning NV) or  $d = 1 \mu\text{m}$  (wide-field)

- (a) Calculate stray field for scanning NV configuration.
- (b) Calculate stray field for wide-field configuration.
- (c) Assess feasibility of wide-field MRAM imaging (refer to Table 16.20 and the warning box in Section 16.6.1).
- (d) Propose array-averaging strategies to improve SNR.

**Hint:** Use Eq. (16.16). Stray field scales as  $1/z^3$ . For wide-field, consider that many MTJs in “1” state contribute coherently.

### Problem 16.5: Production Validation Protocol

Design a golden sample validation protocol for TSV defect detection:

- (a) Specify test structure requirements (geometry, materials, current levels).
- (b) Define measurement sequence and repeat count.
- (c) Establish pass/fail criteria based on Table 16.24.
- (d) Calculate required sample size for 95% confidence in  $\Gamma_{\text{inv}} > 0.85$ .

**Hint:** Use *t*-test for confidence interval. For  $\sigma_{\Gamma_{\text{inv}}} = 0.03$  and target mean  $\Gamma_{\text{inv}} = 0.88$ , sample size  $n \approx 10$  gives 95% CI of  $\pm 0.02$ .

## References

- [16.1] Degen, C. L., Reinhard, F., and Cappellaro, P., “Quantum sensing,” *Reviews of Modern Physics*, vol. 89, no. 3, 035002, 2017.
- [16.2] Barry, J. F., et al., “Sensitivity optimization for NV-diamond magnetometry,” *Reviews of Modern Physics*, vol. 92, no. 1, 015004, 2020.
- [16.3] Rondin, L., et al., “Magnetometry with nitrogen-vacancy defects in diamond,” *Reports on Progress in Physics*, vol. 77, no. 5, 056503, 2014.
- [16.4] Schirhagl, R., et al., “Nitrogen-vacancy centers in diamond: nanoscale sensors for physics and biology,” *Annual Review of Physical Chemistry*, vol. 65, pp. 83–105, 2014.
- [16.5] Kehayias, P., et al., “Imaging crystal stress in diamond using ensembles of nitrogen-vacancy centers,” *Physical Review B*, vol. 100, 174103, 2019.
- [16.6] Taylor, J. M., et al., “High-sensitivity diamond magnetometer with nanoscale resolution,” *Nature Physics*, vol. 4, pp. 810–816, 2008.
- [16.7] Levine, E. V., et al., “Principles and techniques of the quantum diamond microscope,” *Nanophotonics*, vol. 8, no. 11, pp. 1945–1973, 2019.
- [16.8] Wolf, T., et al., “Subpicotesla diamond magnetometry,” *Physical Review X*, vol. 5, 041001, 2015.
- [16.9] Steinert, S., et al., “Magnetic spin imaging under ambient conditions with sub-cellular resolution,” *Nature Communications*, vol. 4, 1607, 2013.
- [16.10] Le Sage, D., et al., “Optical magnetic imaging of living cells,” *Nature*, vol. 496, pp. 486–489, 2013.
- [16.11] Turner, M. J., et al., “Magnetic field fingerprinting of integrated-circuit activity with a quantum diamond microscope,” *Physical Review Applied*, vol. 14, 014097, 2020.
- [16.12] Ku, M. J. H., et al., “Imaging viscous flow of the Dirac fluid in graphene,” *Nature*, vol. 583, pp. 537–541, 2020.
- [16.13] Broadway, D. A., et al., “Improved current density and magnetization reconstruction through vector magnetic field measurements,” *Physical Review Applied*, vol. 14, 024076, 2020.
- [16.14] Hart, C. A., et al., “N-V-diamond magnetic microscopy using a double quantum 4-Ramsey protocol,” *Physical Review Applied*, vol. 15, L021004, 2021.
- [16.15] International Technology Roadmap for Semiconductors (ITRS), “Metrology Chapter,” 2021 Update.
- [16.16] May, P. W., “Diamond thin films: a 21st-century material,” *Philosophical Transactions of the Royal Society A*, vol. 358, pp. 473–495, 2000.
- [16.17] Wagner, K., et al., “Quantum diamond microscopy for semiconductor failure analysis,” in *Proc. ISTFA*, pp. 293–299, 2023.
- [16.18] Healey, A. J., et al., “Quantum microscopy with van der Waals heterostructures,” *Nature Physics*, vol. 19, pp. 87–91, 2023.

- [16.19] Nikawa, K., Inoue, S., Morimoto, K., and Sone, S., “Failure analysis case studies using the optical beam induced resistance change (OBIRCH) method,” in *Proc. International Symposium for Testing and Failure Analysis (ISTFA)*, pp. 394–401, 1999.
- [16.20] Nikawa, K., “Laser-OBIRCH (Optical Beam Induced Resistance Change) technique and its applications to failure analysis of semiconductor devices,” in *Proc. IPFA*, pp. 1–7, 2001.
- [16.21] Schmidt, Ch., Altmann, F., and Breitenstein, O., “Application of lock-in thermography for failure analysis in microsystems and integrated circuits,” *Microelectronics Reliability*, vol. 52, no. 9–10, pp. 2346–2352, 2012.
- [16.22] Breitenstein, O., and Langenkamp, M., *Lock-in Thermography: Basics and Use for Evaluating Electronic Devices and Materials*, 2nd ed., Springer, 2010.
- [16.23] Knauss, L. A., et al., “Scanning SQUID microscopy for current imaging,” *Microelectronics Reliability*, vol. 41, no. 8, pp. 1211–1229, 2001.
- [16.24] Kruth, J.-P., et al., “Computed tomography for dimensional metrology,” *CIRP Annals – Manufacturing Technology*, vol. 60, no. 2, pp. 821–842, 2011.